X-ray beam monitoring and wavelength calibration using four-beam diffraction

XianRong Huang,[a,*] Xianbo Shi[a] and Lahsen Assoufid[a]

[1]*Advanced Photon Source, Argonne National Laboratory, Argonne, Illinois 60439, USA*
*Correspondence e-mail: xiahuang@anl.gov

Abstract

Rigorous dynamical-theory calculations show that four-beam diffraction (4BD) can be activated only by a unique photon energy and a unique incidence direction. Thus, 4BD may be used to precisely calibrate X-ray photon energies and beam positions. Based on the principles that the 4BD pattern, which is typically an X-shaped cross when the main reflection is forbidden, can be generated by instant imaging using the divergent beam from a point source without rocking the crystal, a detailed real-time high-resolution beam position monitoring scheme is illustrated for monitoring two-dimensional beam positions and directions of modern synchrotron light sources, X-ray free electron lasers and nano-focused X-ray sources.

1. Introduction

X-ray diffraction from crystals is generally based on Bragg's law of two-beam diffraction (2BD), $2d\sin\theta = \lambda$, where θ is the Bragg angle, λ is the X-ray wavelength, and d is the spacing of the diffracting lattice planes. If λ can continuously vary, Bragg diffraction may occur at any angle $0 < \theta \leq 90°$ with no special points (DuMond, 1937). Therefore, without references, it is challenging to use Bragg diffraction to accurately calibrate/measure X-ray wavelengths (photon energies) or beam directions since it is usually difficult to measure θ with very high precision. As an alternative, X-ray absorption edges of elements have been widely used for wavelength calibration, particularly for double-crystal monochromators (DCMs) of synchrotron beamlines (Kraft *et al*., 1998). However, the absorption edges are usually very wide (up to a few tens of electron volts) (Keski-Rahkonen & Krause, 1974) and meanwhile may have complicated structures, which results in low precision in most cases.

The other disadvantage of Bragg diffraction is that it is only very sensitive to the incidence angle θ angle but insensitive to the lateral φ angle along the direction perpendicular to the *plane of incidence* (the plane containing both the principal incident wavevector and the crystal surface normal). In other words, Bragg's law of 2BD is mainly a one-dimensional (1D) equation that is unable to generate two-dimensional (2D) diffraction patterns required to precisely determine the 2D position and direction of an X-ray beam in space.

To overcome these problems, it has been proposed to use multiple-beam diffraction as a means to calibrate photon energies (e.g., Arthur, 1989; Hagelstein *et al.*, 1992). However, these methods as well as almost all the existing multiple-beam diffraction methods involve (wide-range) Φ-scans that have extremely low resolution because the lateral beam divergence is generally much larger than the divergence along the θ angle for conventional X-ray sources. For this reason, the 4th-generation synchrotrons (e.g., Pacchioni, 2019) and X-ray free electron lasers (XFELs) (e.g., Emma *et al.* 2010) with small 2D source sizes that can produce X-ray beams with high 2D collimation are expected to renew scientists' interest in research and applications of multiple-beam diffraction. Here we illustrate a detailed scheme that may accurately calibrate the wavelengths of X-ray beams and at the same time monitor their 2D positions and directions. The scheme is based on forbidden-reflection four-beam diffraction (4BD) from crystals with cubic structures, which can be activated by a unique photon energy and a unique beam direction. For a point source, the 4BD pattern is an X-shaped cross that can be generated by imaging without rocking the crystal. Therefore, this unique property can be used for real-time monitoring of the beam positions. Compared to other diffraction-based beam position monitoring (BPM) methods (e.g., Samadi *et al.*, 2015; Samadi *et al*., 2019*a*, 2019*b*), the 4BD method achieves much higher precision. In particular, it can reveal the 2D position of the source and the 2D angular direction of the X-ray beam simultaneously. This 4BD method may be particularly well-suited for applications for modern synchrotron light sources, XFELs, and nano-focused beams that have very small source sizes in both horizontal and vertical directions.

2. Four-beam diffraction patterns and properties

To demonstrate the concept, we studied 4BD using silicon $000/006/113/1\bar{1}3$ reflections with the lattice constant $a_0 = 5.431$ Å. For a synchrotron X-ray source, this diffraction process can be activated by restricting the incident beam in the plane parallel to the (010) lattice plane, as shown

in Fig. 1(a). Then by varying the incidence angle θ while keeping the incidence wavelength λ satisfying the Bragg condition of the 006 reflection,

$$\lambda = (a_0/3)\sin\theta, \tag{1}$$

for specific wavelengths, some reciprocal lattice points may also fall on the Ewald sphere of reflection 006. Under this condition, multiple-beam diffraction occurs (Chang, 2004; Colella, 1974). For example, if the reciprocal lattice point 113 is on the Ewald sphere [Fig. 1(b)], it is obvious that the angle between its diffraction vector $\mathbf{g}_2 = a_0^{-1}(\hat{\mathbf{x}} + \hat{\mathbf{y}} + 3\hat{\mathbf{z}})$ and the incident wavevector $\mathbf{K}_0 = \lambda^{-1}(\cos\theta\,\hat{\mathbf{x}} - \sin\theta\,\hat{\mathbf{z}})$ is $\pi/2 + \theta_{113}$, i.e.,

$$\frac{\mathbf{K}_0\cdot\mathbf{g}_2}{|\mathbf{K}_0||\mathbf{g}_2|} = -\sin\theta_{113}, \tag{2}$$

where θ_{113} is the Bragg angle of reflection 113 satisfying

$$2a_0(1^2 + 1^2 + 3^2)^{-1/2}\sin\theta_{113} = \lambda, \tag{3}$$

and $\hat{\mathbf{x}}$, $\hat{\mathbf{y}}$, $\hat{\mathbf{z}}$ are unit vectors along the [100], [010], [001] directions, respectively. Then one can obtain $\theta = 40.6013°$ from equations (1)-(3). We denote this angle by θ_{4B}. The corresponding photon energy is $E_{4B} = 10.5236$ keV. By symmetry, the $1\bar{1}3$ reciprocal lattice point is also located on the Ewald sphere when $\mathbf{K}_0$ lies in the (010) plane. Therefore, under these conditions, Fig. 1 represents a 4BD configuration involving reflections 000, 006, 113 and $1\bar{1}3$ (Huang *et al*., 2014*a*, 2014*b*), and we call $\mathbf{g}_1 = 006$ the *main* reflection.

Here, we are only interested in the diffraction intensity of the main reflection $\mathbf{g}_1 = 006$ along the $\mathbf{K}_1$ direction in Fig. 1. This implies that the experimental 4BD setup will be almost identical to that of 2BD, where one sets the detector to collect only the main reflection intensity (pattern). The intensities of the other two reflections $\mathbf{g}_2 = 113$ and $\mathbf{g}_3 = 1\bar{1}3$ are usually of no importance. The only difference is that 4BD requires a high-resolution (~ 1 μrad or better) rotation stage for accurate control of the azimuthal angle Φ in Fig. 1, while in 2BD, the diffraction pattern is invariant with Φ for symmetric reflections.

Another interesting property of multiple-beam diffraction is that some of the involved reflections can be forbidden reflections. For the $000/006/113/1\bar{1}3$ 4BD case, the main reflection 006 of silicon is forbidden, but it can still produce strong diffraction along $\mathbf{K}_1$ direction in Fig. 1. The underlying mechanism is that the diffraction intensity along $\mathbf{K}_1$ comes from two *detour reflection channels* in Fig. 1(b). In one channel, the incident beam is first diffracted by $\mathbf{g}_2$, i.e., $\mathbf{K}_0 + \mathbf{g}_2 = \mathbf{K}_2$. Then this diffracted wave is further diffracted by $\mathbf{g}_2' = \mathbf{g}_1 - \mathbf{g}_2 = \bar{1}\bar{1}3$ to produce a diffracted wave with wavevector $\mathbf{K}_1$, i.e., $\mathbf{K}_2 + \mathbf{g}_2' = \mathbf{K}_1$. Similarly, the other channel consists of the two steps $\mathbf{K}_0 + \mathbf{g}_3 = \mathbf{K}_3$ and $\mathbf{K}_3 + \mathbf{g}_3' = \mathbf{K}_1$, where $\mathbf{g}_3' = \mathbf{g}_1 - \mathbf{g}_3 = \bar{1}13$ (Huang *et al*., 2014*a*, 2014*b*). Since the direct diffraction channel $\mathbf{K}_0 + \mathbf{g}_1 = \mathbf{K}_1$ is forbidden, the diffraction pattern detected along the $\mathbf{K}_1$ direction is a pure multiple-beam diffraction effect without the contribution of direct 2BD. Nevertheless, the mechanism illustrated in the following also applies to the case where $\mathbf{g}_1$ is not forbidden, but for such cases, the strong direct $\mathbf{g}_1$ diffraction intensity may significantly reduce the visibility of the 4BD pattern.

X-ray multiple-beam diffraction from perfect crystals can be rigorously computed by the *Fourier coupled-wave diffraction theory* (FCWDT) (Huang *et al*., 2013), which is based on similar principles as the method developed by Stetsko & Chang (1997). But, the FCWDT is more efficient and accurate. Using the FCWDT, we have calculated the 2D distribution of the reflectivity R_1

along the $\mathbf{K}_1$ direction for the $000/006/113/1\bar{1}3$ 4BD configuration, as shown in Fig. 2. Here we always set the main reflection to be symmetric, i.e., $\mathbf{g}_1$ is strictly perpendicular to the crystal surface. We allow the incident beam to slightly deviate from the (010) plane by an azimuthal angle Φ. Then the incident wavevector can be written as $\mathbf{K}_0 = \lambda^{-1}(\cos\theta\cos\Phi\,\hat{\mathbf{x}} + \cos\theta\sin\Phi\,\hat{\mathbf{y}} - \sin\theta\,\hat{\mathbf{z}})$ in Fig. 1. The reflectivity only depends on $\mathbf{K}_0$, i.e., R_1 is a function of Φ, θ, and the photon energy E. Fig. 2(b) shows the calculated R_1 distribution as a function of Φ and θ at the exact Bragg energy $E_{4B} = 10.5236$ keV. $\Delta\theta$ is the relative deviation of the incidence angle from the geometrical Bragg angle $\theta_{4B} = 40.6013°$. This map represents a 2D "rocking curve" for an incident plane wave.

Note that for 2BD, the Bragg condition is maintained when the incident and diffracted beams are rotated around the diffraction vector. We call the cone formed by such rotation the *diffraction cone*. For example, azimuthal rotation of $\mathbf{K}_0$ and $\mathbf{K}_1$ along $\mathbf{g}_1$ in Fig. 1(a) forms a cone that is the diffraction cone of $\mathbf{g}_1$. The diffraction pattern in Fig. 2(b) mainly consists of three lines, which correspond to the diffraction cones of the three reflections 006, 113 and $1\bar{1}3$, respectively, in the Φ-θ coordinate system. For example, the horizontal line corresponds to the 006 reflection, of which the Bragg condition is independent of the Φ angle. All the three lines intersect in the central region that is the 4BD region. In this region, the three lines have significant distortions, indicating that the three reflections have strong interactions. Here also note that the detour reflection can be very strong, with reflectivity close to 100% in some central regions although the direct 006 reflection is forbidden.

Fig. 2(a) is the diffraction pattern when the photon energy E deviates from E_{4B} by $\Delta E = -0.5$ eV. Consequently, the Bragg angle of the 006 reflection increases following equation (1), as indicated by the upward shift of the 006 diffraction line (cone). The 113 and $1\bar{1}3$ diffraction cones also change with E according to their respective Bragg equations, for instance, equation (3) for reflection 113. The resulting effect is that the three lines no longer intersect at the same point, indicating that the 4BD condition can not be satisfied when the incident energy deviates from E_{4B}. Instead, each pair of lines intersect at a distinct point that corresponds to a three-beam diffraction (3BD) process (Renninger, 1937; Lang *et al*., 2013). The top-left (T_1) and top-right intersections in Fig. 2(a) correspond to the $000/006/113$ and $000/006/1\bar{1}3$ 3BD processes, respectively, while the intersection in the central area corresponds to $000/113/1\bar{1}3$ 3BD. Fig. 2(c) is the diffraction pattern for photon energy $E = E_{4B} + 0.5$ eV, and it is nearly a mirror image of Fig. 2(a) with respect to the central 006 diffraction line $\Delta\theta = 8$ μrad in Fig. 2(b). Here the slight shift of the central line from $\Delta\theta = 0$ in Fig. 2(b) is caused by the slight refraction effect of X-rays.

The most important phenomenon revealed from Fig. 2 is that 4BD can only occurs along a unique incidence direction and for a unique photon energy. For the current case, the unique energy is $E_{4B} = 10.5236$ keV, which is determined only by the lattice constant a_0. The unique incidence direction corresponds to $\Delta\theta = 8$ μrad (relative to $\theta_{4B} = 40.6013°$) and $\Phi = 0$ [relative to the (010) lattice plane].

Fig. 2 shows that the plane-wave 4BD pattern is very sensitive to photon energy variation. For a real X-ray beam, the spectrum always has a finite energy bandwidth. Here we consider a synchrotron radiation beam monochromatized by an upstream Si (111) DCM. The spectral bandwidth of the beam after the DCM is about 1.5 eV at 10.5 keV, and we assume the intensity has a Gaussian distribution in E. Based on such an incident beam, we have computed the plane wave diffraction patterns (as in Fig. 2) for different energies within the DCM bandwidth and

overlapped them together to form the integrated diffraction pattern in Fig. 3(a). Here the center of the Gaussian spectrum is E_{4B}. The pattern is an X-shaped cross consisting of two oblique bands. Here note that the central lines of the two bands (dashed lines) are not the diffraction cones in Fig. 2. The diffraction cones in Fig. 2 are for monochromatic beams, and their cone apertures ($2\theta_B$) vary with the photon energy E according to their respective Bragg equations, as indicated by the displacements of the lines with E in Fig. 2. In contrast, the two oblique dashed lines in Fig. 3 have fixed positions although the diffraction intensity distribution on the lines changes with varying E. The other obvious difference is that the oblique lines in Figs. 2 and 3 have different slopes.

Detailed analyses show that the two dashed lines in Fig. 3 are the loci of the monochromatic $000/006/113$ and $000/006/1\bar{1}3$ 3BD centers for different photon energies. For examples, the line intersection centers T_1 and T_2 in Fig. 2 are indeed located on the two dashed lines in Fig. 3(a). Such intersections move in the Φ-θ coordinate system with varying E, thus forming the two 3BD lines that can extend far away if the energy and angular ranges are wide enough. Based on this conclusion, one can use the Bragg equations and equations (2) to easily calculate the slopes and positions of dashed lines in the Φ-θ space. On the other hand, this indicates that 3BD can continuously occur for any wavelengths allowed by the diffraction geometry, similar to 2BD. Hence, 3BD usually cannot be used for energy calibration. However, the intersection of the two dashed line in Fig. 3, here called the *cross center* (CC), is the 4BD center that corresponds to a unique photon energy and a unique incidence direction even for polychromatic incident beams. This can be seen from Fig. 3(b) and 3(c) that when the central energy of the incident Gaussian spectrum deviates from E_{4B}, the strong diffraction regions move away from the fixed-position CC to cover different regions of the X-shaped cross. The strong diffraction centers are always on the two fixed dashed lines. Here it can be verified that the shift of the strong diffraction center from the CC, $\Delta\Theta$, along the $\Delta\theta$ axis [see Fig. 3(c)] and the shift of the spectral center, ΔE, satisfy the differential Bragg law of the 006 reflection,

$$\Delta\Theta/\tan\theta_{4B} = -\Delta E/E_{4B} \tag{4}$$

around θ_{4B}. Hence, different points with different θ angles on the dashed lines correspond to different energies. Only those points with the corresponding energies falling within the incident spectrum can have strong diffraction when the incidence direction is correct, while the other points corresponding to energies out of the spectrum will not diffract for any incidence directions. If E is further away from E_{4B}, the CC may be completely out of diffraction. In such circumstances, one can still extrapolate the measured dashed line segments [e.g., in the lower half of Fig. 3(c)] to derive the CC position. This is very useful for the initial search and alignment of the 4BD crystal orientation (and also for monitoring X-ray beams with large variations).

Therefore, a polychromatic incident beam can produce a unique X-shaped diffraction pattern in the vicinity of the 4BD conditions. In particular, the spectral bandwidth and the divergence of the incident beam only affect the extent of the diffraction pattern (in the Φ-θ space) and its intensity distribution without affecting the position of the CC. But, note that a white beam will not work here since it will activate strong harmonic reflections, such as 004 and 008, that will significantly reduce (if not destroy) the visibility of the 006 reflection. This is the reason why we have considered in the above a synchrotron beam monochromatized by a Si (111) DCM.

Thus, we have illustrated that practical 4BD experiments with finite-bandwidth incident beams can be used to calibrate X-ray photon energies and measure the directions of X-ray beams based on the fact that the CC in Fig. 3 corresponds to a unique energy and a unique incidence direction.

Although the polychromatic diffraction patterns are not as sharp as the plane-wave diffraction patterns, it is evident that the energy resolution can reach the sub-eV level or better from the comparison of the three patterns in Fig. 3, which is more accurate than the absorption edges. Meanwhile, the angular resolution can reach the μrad level. In particular, the beam directions determined by 4BD are complete 2D orientations (with the same high resolution along both the θ and Φ directions), which is a remarkable advantage over 2BD that is only sensitive to the 1D directional change $\Delta\theta$.

3. Energy calibration and beam position monitoring of point sources

In principle, the diffraction patterns in Fig. 3 can be realized by 2D rocking of the crystal near the 4BD conditions using a parallel polychromatic (but not white) incident beam, but such a 2D scanning process will be quite time-consuming. Meanwhile, X-ray beams with 2D high collimation are very difficult to obtain and most X-ray beams have larger lateral (φ) divergence as aforementioned. In the following, we will focus on the principles of an imaging method that uses a naturally divergent beam from a point source without any collimation to form a one-shot image of the 4BD pattern.

First, note that symmetric Bragg reflections always obey the flat mirror reflection (specular reflection) law for ray directions, which results from the conservation of the tangential momenta, $\mathbf{K}_{0||} + \mathbf{g}_{n||} = \mathbf{K}_{n||}$. Here || denotes the tangential component of the corresponding vector, i.e., the projection of the vector onto the crystal surface. This equation is valid for any Bragg reflection (Huang *et al*., 2013). For the symmetric main reflection $\mathbf{g}_1$ in Fig. 1, $\mathbf{g}_{1||} = 0$ leads to $\mathbf{K}_{1||} = \mathbf{K}_{0||}$. Consequently, $|\mathbf{K}_1| = |\mathbf{K}_0|$ gives $K_{1z} = -K_{0z}$. For symmetric Bragg reflections (of either two- or multiple-beam diffraction), this mirror reflection law is always valid *for any incidence directions and any wavelengths*. [Asymmetric reflections are dispersive and do not have this property (Huang *et al*., 2011).] In the case of a point source, therefore, the symmetric Bragg reflection gives rise to a mirror-image virtual source S', as shown in Fig. 4(a). Viewed from S', each ray will not change its direction at all during the Bragg reflection. The only difference of the Bragg reflection is that only X-rays falling within a narrow spectral bandwidth and in a very small angular range will be strongly reflected, while mirror reflection of light is usually achromatic for any incidence direction. Similarly, a DCM consisting of two identical symmetric reflections also exactly preserves the direction of each ray, where the second reflection exactly offsets the deflection angle of the first one. The net effect is that the DCM only causes a beam displacement that has no effect on the subsequent imaging process.

Second, the 2D orientation of a ray emitted from a point source can be described by two small angles along two orthogonal directions $\Delta\theta$ and φ with respect to the central axis of the beam, as shown in Fig. 4(b). For synchrotron beamlines, these two directions usually correspond to the vertical and horizontal divergence directions, respectively. For vertical Bragg reflections, the vertical divergent angle $\Delta\theta$ is the same as the variation of the incidence angle θ on the crystal surface in Fig. 4(b). In addition to θ, we have also used the azimuthal angle Φ above in Figs. 2 and 3 to describe the incidence wavevector $\mathbf{K}_0 = \lambda^{-1}(\cos\theta\cos\Phi\,\hat{\mathbf{x}} + \cos\theta\sin\Phi\,\hat{\mathbf{y}} - \sin\theta\,\hat{\mathbf{z}})$. From Fig. 4(b) it is apparent that the lateral (horizontal) divergence angle φ is proportional to the azimuthal angle Φ we used in the above calculations by a geometrical factor $\cos\theta_{4B}$, i.e., $\varphi = \Phi\cos\theta_{4B}$ for small φ. For the current case, $\cos\theta_{4B} = 0.76$.

Hence, a point source naturally provides X-rays along all the various directions around the central axis of the beam. When the divergent beam is incident on the crystal, each point on the illuminated surface corresponds to a unique incidence direction (φ, θ). Consequently, the point source may generate the 4BD patterns in Fig. 3 as one-shot images without the necessity of 2D angular scans of the crystal. In Fig. 3, we have set the $\Delta\theta$ and φ (top) axes to have the same scale. Then the one-shot images will have exactly the same shapes as the simulated images if the imaging device (usually a charge-coupled device, CCD) is set perpendicular to the diffracted beam. As shown in Fig. 4(a), if we establish the XZ coordinate system on the CCD, the positions on the CCD are related to the angular directions by $X = D\varphi$ and $Z = D\Delta\theta$, where D is the distance between the point source and the CCD. If we assume $D = 50$ m for a synchrotron beamline, the image size in Fig. 3 will be 3.5×1.3 cm^2, which is close to the fields of view of some typical X-ray CCDs. If the beam divergence is smaller than that in Fig. 3, one can adjust the DCM and the crystal to image only the central part of the diffraction pattern.

The above principles show that a point source can be used to perform real-time imaging of the 2D 4BD pattern without angular scans of the crystal. In experiments, one can first set the DCM energy roughly at E_{4B} and set the Bragg angle of $\mathbf{g}_1 = 006$ at θ_{4B}. Here since the main reflection $\mathbf{g}_1$ is forbidden, initial alignment of the crystal to the exact 4BD conditions may be challenging. It may require both the Φ scan and the DCM energy scan at the same time to find two symmetric 3BD points on the two oblique dashed lines, respectively (with the same $\Delta\theta$ angle). From these two points the CC can be calculated based on the slopes of the two dashed lines in the Φ-θ coordinate system. Then one can set the crystal orientations to the calculated CC positions and make further fine adjustments of the DCM energy and the crystal orientation till the symmetric 4BD image in Fig. 3(a) is obtained. Under this condition, the DCM energy (center of the spectrum) is calibrated to E_{4B} with an accuracy better than 0.5 eV. Meanwhile, the crystal orientation is also precisely determined.

In practice, the finite source size may blur the images in Fig. 3. However, for modern low-emittance synchrotron light sources or XFELs with source sizes $\Delta s < 50$ μm and beamline lengths $D > 10$ m, the source size effect $\Delta s/D < 5$ μrad is very small, which can be further reduced or eliminated by image processing and data fitting. For the studied case, from data fitting the energy calibration precision may reach 0.1 eV or better. In a reversed way, data fitting of the image blurring can also give information about the source size.

In addition to wavelength calibration, the most important potential application of the 4BD setup is for BPM of modern synchrotron light sources and XFELs, and the principles can be understood from Fig. 5. In Fig. 5(a), we assume that the DCM and the crystal are accurately aligned to the 4BD conditions to produce a symmetric 4BD pattern on the CCD detector. For simplicity of description, we further assume that the thick red line connecting the (virtual) source and the CC of the 4BD pattern is exactly horizontal. After the initial alignment, we assume that the DCM and the crystal are strictly static. Now in Fig. 5(b) if the source is displaced in the transverse plane by a distance Δh, the horizontal red line containing the source will also be displaced by Δh. As described above, the CC of the 4BD pattern always corresponds to an exact unique incidence direction, which is the horizontal direction here. This indicates that the CC on the CCD will also be displaced by the same Δh. Hence, the CC on the CCD will move synchronously with the source along the same direction with the same magnitude. Therefore, monitoring the movement of the CC on the CCD is equivalent to real-time monitoring of the beam/source position. If the resolution of

the CCD is on the micrometer level, it is expected that this BPM method can achieve micrometer resolution. Data fitting may further improve the spatial resolution.

As shown by Samadi *et al.* (2015), not only the position of a synchrotron light source or XFEL may vary over time, but the beam direction (angle) can also change. Fig. 5(c) schematically shows that the X-ray beam has both a displacement Δh and an orientation change $\Delta\alpha$. It is obvious that as long as the horizontal direction remains within the angular range of the divergent beam, the additional $\Delta\alpha$ does not affect the displacement of the CC, which is still Δh. Under the condition that the beam divergence is small enough, however, the angular variation of the beam will make the 4BD pattern asymmetric with the image center (which can be calculated by data fitting if necessary) shifted from the CC by a distance of $\Delta c = D\Delta\alpha$ if the divergence of the beam is small enough. If the beam divergence is large, measurements of Δc may not be very accurate. Meanwhile, the variation of the 4BD pattern from the symmetric shapes in Figs. 5(a) and 5(b) caused by beam direction changes may also depend on the spectrum (which can be numerically computed). However, all these factors do not affect the beam position variation Δh if the beam direction variation remains reasonably small. (For large beam direction variation, the 4BD could be out of the angular range of the incident beam.)

For simplicity, the variations of the beam and the image in Fig. 5 are schematically indicated by the 1D movements of the images, but it is obvious that in experiments the image variation gives the 2D variations of the source position and beam directions since the 4BD pattern is a 2D cross. As mentioned above, this is a remarkable advantage over 2BD schemes that can only give 1D beam position variation.

4. Discussion and conclusion

The above principles of 4BD and the corresponding point source imaging scheme are based on rigorous dynamical theory calculations. A practical implementation of the scheme at a synchrotron beamline for BPM will be two challenging requirements. The first is to maintain high stability of the DCM, particularly the stability of the relative orientation between the two DCM crystals. Variation of this relative orientation directly alters the virtual source position. It also changes the spectrum and beam direction, although these two factors are less critical than the virtual source variation that directly affects the precision and reliability of the BPM. On the other hand, by frequency analyses, it is also possible to decouple and identify the origin of beam motion (vibration) from either the source or the optics (Samadi *et al.*, 2019).

The second requirement is to reduce the heat load of the DCM so as to make the crystals free of thermal lattice distortion or minimize it as much as possible (better than 10^{-5}). Lattice distortion (similar to slope errors of mirrors) will significantly change the directions of the locally diffracted X-rays and thus change the virtual source size and position, which may significantly affect or even destroy the 4BD pattern. A possible way to mitigate the heat load is to use a thin-crystal window as a beam splitter to diffract a weak beam for the 4BD imaging setup, as schematically shown in Fig. 6. This scheme has three major advantages. First, the head load of the thin crystal may be very small since the crystal thickness can be as thin as a few micrometers such that most of the photons will be transmitted without absorption. (Setting homogeneous absorbers/filters upstream the thin crystal may reduce the long-wavelength heat load.) Second, the spectral bandwidth of the beam diffracted by the thin crystal can be wider than that diffracted by a thick crystal. The wide

bandwidth can extend the angular range of the 4BD pattern in Fig. 3 (but must not be so wide to activate harmonic reflections of $\mathbf{g}_1$). Third, it is apparent that with the use of a thin-crystal splitter, the 4BD-based BPM process will not require a dedicated beamline. Hence it may be implemented at any beamline with little effect on the main beamline.

Although the studied case focused on the 4BD case around 10 keV, there are, in fact, a large number of such 4BD configurations that cover various energies. For $E < 20$ keV, Table 1 lists some typical 4BD cases of silicon with a (001) surface and with the same (010) plane of incidence. Note that one can use a single silicon crystal with the (001) surface to realize all these 4BD configurations simply by setting the Bragg angle of the main reflection ($\mathbf{g}_1 = 002$ or 006) to the specific θ_{4B}. If the crystal is rotated by 45° such that the plane of incidence becomes (110) plane that also has mirror symmetry, we can obtain another set of 4BD configurations. Overall, the density of 4BD cases for $E > 10$ keV is high so that one can find a 4BD case close to almost any photon energy.

In fact, some of the special 4BD configurations in Table 1 involve six or eight reflections (or more). For such six- and eight-beam diffraction geometry, the diffraction patterns consist of three and four lines, respectively, instead of only two lines in Fig. 3 for 4BD. All these lines intersect at the same point that is the center of the diffraction pattern as in Fig. 3(a). Therefore, the diffraction mechanisms of six- or eight-beam diffraction is almost the same as 4BD for energy calibration and for BPM. As mentioned above, the slopes and positions of all the inclined lines can be calculated by a simple computer program using simple geometry without the complicated dynamical theory calculations. This will make it convenient for one to choose suitable reflections in practical applications of the current multiple-beam diffraction scheme.

The 4BD principles are also valid for the case where $\mathbf{g}_1$ is not forbidden. In this circumstance, however, the 4BD pattern has a strong and wide vertical column that is the mainly the direct two-beam diffraction intensity of $\mathbf{g}_1$ (nearly independent of Φ in the regions away from the CC). This column will greatly reduce or hide the sharp contrast features around the CC in Fig. 3.

Table 1. Typical 4BD reflections from the silicon (001) surface for $E < 20$ keV.

4BD reflections	$\boldsymbol{\theta_{4B}}$ **(°)**	$\boldsymbol{E_{4B}}$ **(keV)**
$000/002/\bar{1}11/\bar{1}\bar{1}1$	63.4349	2.55235
$000/002/\bar{3}11/\bar{3}\bar{1}1$	33.6901	4.11554
$000/002/\bar{3}1\bar{1}/\bar{3}\bar{1}\bar{1}$	24.7751	5.44767
$000/002/\bar{1}13/\bar{1}\bar{1}3$	21.8014	6.14687
$000/006/\bar{3}33/\bar{3}\bar{3}3$	63.4349	7.65705
$000/006/\bar{3}31/\bar{3}\bar{3}1$	54.1623	8.44807
$000/006/\bar{5}31/\bar{5}\bar{3}1$	45.9710	9.52543
$000/006/113/1\bar{1}3$	40.6013	10.5236
$000/006/\bar{5}53/\bar{5}\bar{5}3$	36.1932	11.5979
$000/006/\bar{7}53/\bar{7}\bar{5}3$	32.8687	12.6193
$000/006/\bar{7}55/\bar{7}\bar{5}5$	31.3287	13.1719
$000/006/\bar{9}53/\bar{9}\bar{5}3$	29.1047	14.0801
$000/006/\bar{7}57/\bar{7}\bar{5}7$	27.4076	14.8782
$000/006/\bar{9}57/\bar{9}\bar{5}7$	25.5420	15.8838

000/006/$\bar{7}$75/$\bar{7}\bar{7}$5	24.3045	16.6397
000/006/$\bar{7}$59/$\bar{7}\bar{5}$9	22.5796	17.8367
000/006/$\bar{9}$77/$\bar{9}\bar{7}$7	21.5124	18.6764
000/006/$\bar{5}$77/$\bar{5}\bar{7}$7	20.3231	19.7189

In summary, we have used rigorous dynamical-theory calculations to demonstrate that the forbidden-reflection 4BD pattern, which is typically an X-shaped cross, can be activated only by a unique photon energy and a unique incidence direction. The 4BD geometry can be used to precisely calibrate photon energies and X-ray beam positions (and directions). Based on the principles that the 4BD pattern can be generated by direct imaging using the divergent beam from a point source without crystal rocking, we illustrated a high-resolution beam position monitoring scheme for real-time monitoring or ultrafast imaging of the sources of modern synchrotron beamlines (including all bending-magnet, wiggler, and undulator beamlines), and XFELs, as well as nano-focused beams.

Acknowledgements: This work was supported by the U.S. Department of Energy, Office of Science, Office of Basic Energy Sciences, under contract No. DE-AC02-06CH11357.

References:

Arthur, J. (1989). *Rev. Sci. Instrum.* **60**, 2062-2063.

Chang, S.-L. (2004). *X-ray Multiple-Wave Diffraction: Theory and Applications*, Solid State Sciences Series, Vol. 143. Berlin: Springer-Verlag.

Colella, R. (1974). *Acta Cryst.* A**30**, 413–423.

DuMond, J. (1937). *Phys. Rev.* **52**, 872–883.

Emma, P. *et al.* (2010), Nat. Photonics **4**, 641-647.

Hagelstein, M., Cunis, S., Frahm, R. & Rabe, P. (1992). *Rev. Sci. Instrum.* **63**, 911-913.

Huang, X. R., Macrander, A. T., Honnicke, M. G., Cai, Y. Q. & Fernandez, P (2011). *J. Appl. Cryst.* **45**, 255-262.

Huang, X.-R., Jia, Q., Wieczorek, M. & Assoufid, L. (2014*a*). *J. Appl. Cryst.* **47**, 1716-1721.

Huang, X.-R., Peng, R.-W., Gog, T., Siddons, D. P. & Assoufid, L. (2014*b*). *Appl. Phys. Lett.* **105**, 181903.

Huang, X.-R., Peng, R.-W., Hönnicke, M. G. & Gog, T. (2013). *Phys. Rev. A* **87**, 063828.

Keski-Rahkonen, O. & Krause, M. O. (1974). *At. Data Nucl. Data Tables* **14**, 139–146.

Kraft, S., Stümpel, J., Becker, P. & Kuetgens, U. (1996). *Rev. Sci. Instrum.* **67**, 681-687.

Lang, R., de Menezes, A. S., dos Santos, A. O., Reboh, S., Meneses, E. A., Amaral, L. & Cardoso, L. (2013). *J. Appl. Cryst.* **46**, 1796-1804.

Pacchioni, G. (2019). *Nat. Rev. Phys.* **1**, 100–101.

Samadi, N., Bassey, B., Martinson, M., Belev, G., Dallin, L., de Jong, M. & Chapman, D. (2015). *J. Synchrotron Rad.* **22**, 946-955.

Samadi, N., Shi, X., Dallin, L. & Chapman, D. (2019*a*). *J. Synchrotron Rad.* **26**, 1213-1219.

Samadi, N., Shi, X. & Chapman, D. (2019*b*). *J. Synchrotron Rad.* **26**, 1863-1871.

Samadi, N., Shi, X., Dallin, L. & Chapman, D. (2019*c*). *Phys. Rev. Accel. Beams* **22**, 122802.
Stetsko, Y. P. & Chang, S.-L. (1997). *Acta Cryst. A* **53**, 28-34.
Renninger, M. (1937). *Z. Phys. A Hadrons Nucl.* **106**, 141–176.

Figures and Captions

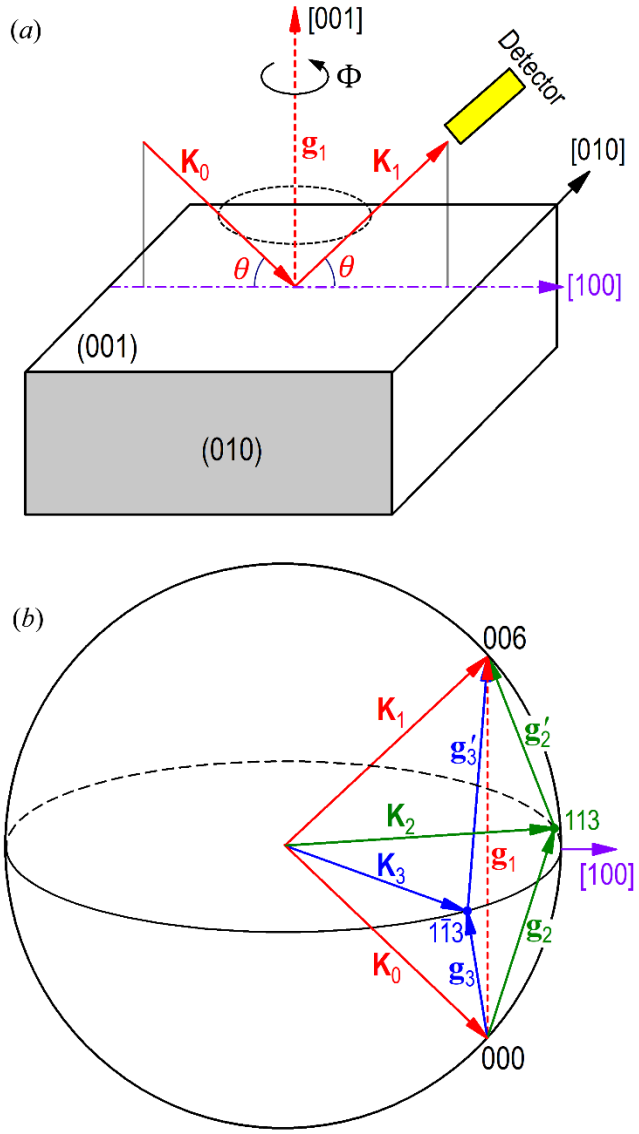

Figure 1. (a) Diffraction geometry of the 006 main reflection in the $000/006/113/1\bar{1}3$ 4BD configuration with the plane of incidence parallel to (010). $\mathbf{K}_0$ is the incidence wavevector, and $\mathbf{K}_1$ is the 006 reflection wavevector. The dashed circle indicates the diffraction cone of $\mathbf{g}_1$ formed by rotation of $\mathbf{K}_0$ and $\mathbf{K}_1$ around $\mathbf{g}_1$. (b) Configuration of the Ewald sphere in reciprocal space. The four reciprocal lattice points 000, 006, 113 and $1\bar{1}3$ are all on the Ewald sphere. $\mathbf{g}_1 = \mathbf{g}_2 + \mathbf{g}'_2 = \mathbf{g}_3 + \mathbf{g}'_3$.

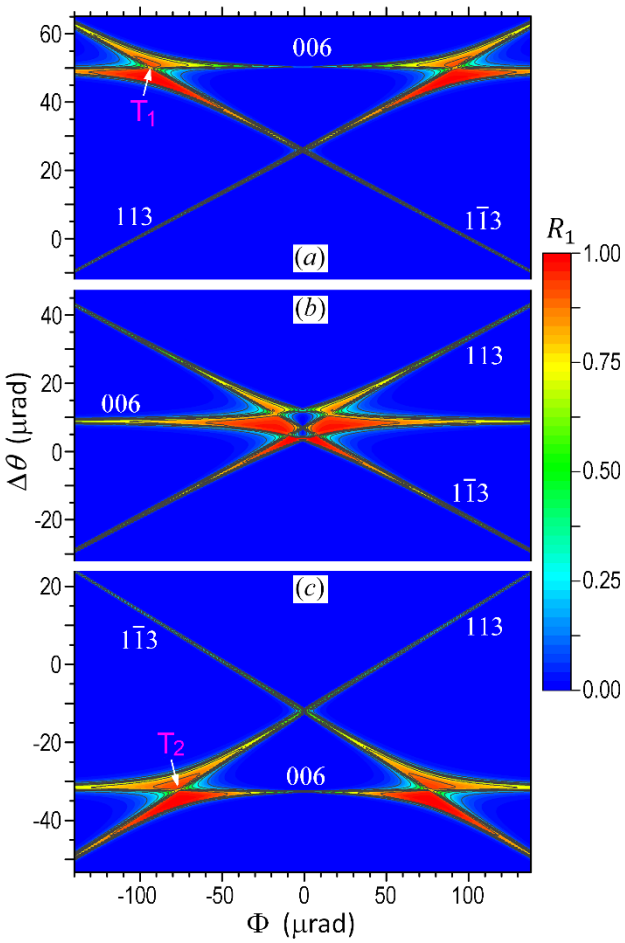

Figure 2. Computed 2D "rocking curve" of the $000/006/113/1\bar{1}3$ 4BD setup in Fig. 1 showing the reflectivity R_1 of the main reflection $\mathbf{g}_1 = 006$ as a function of the incidence angle $(\Phi, \Delta\theta)$ and the photon energy E. The indices of each line (diffraction cone) indicate the corresponding Bragg reflection. σ-polarization, i.e., the electric field of the incident wave is parallel to [010] in Fig.1(a). Semi-infinite Si crystal. $\Delta\theta = 0$ always corresponds to $\theta_{4B} = 40.6013°$. (a) $E = E_{4B} - 0.5$ eV. (b) $E = E_{4B}$. (c) $E = E_{4B} + 0.5$ eV.

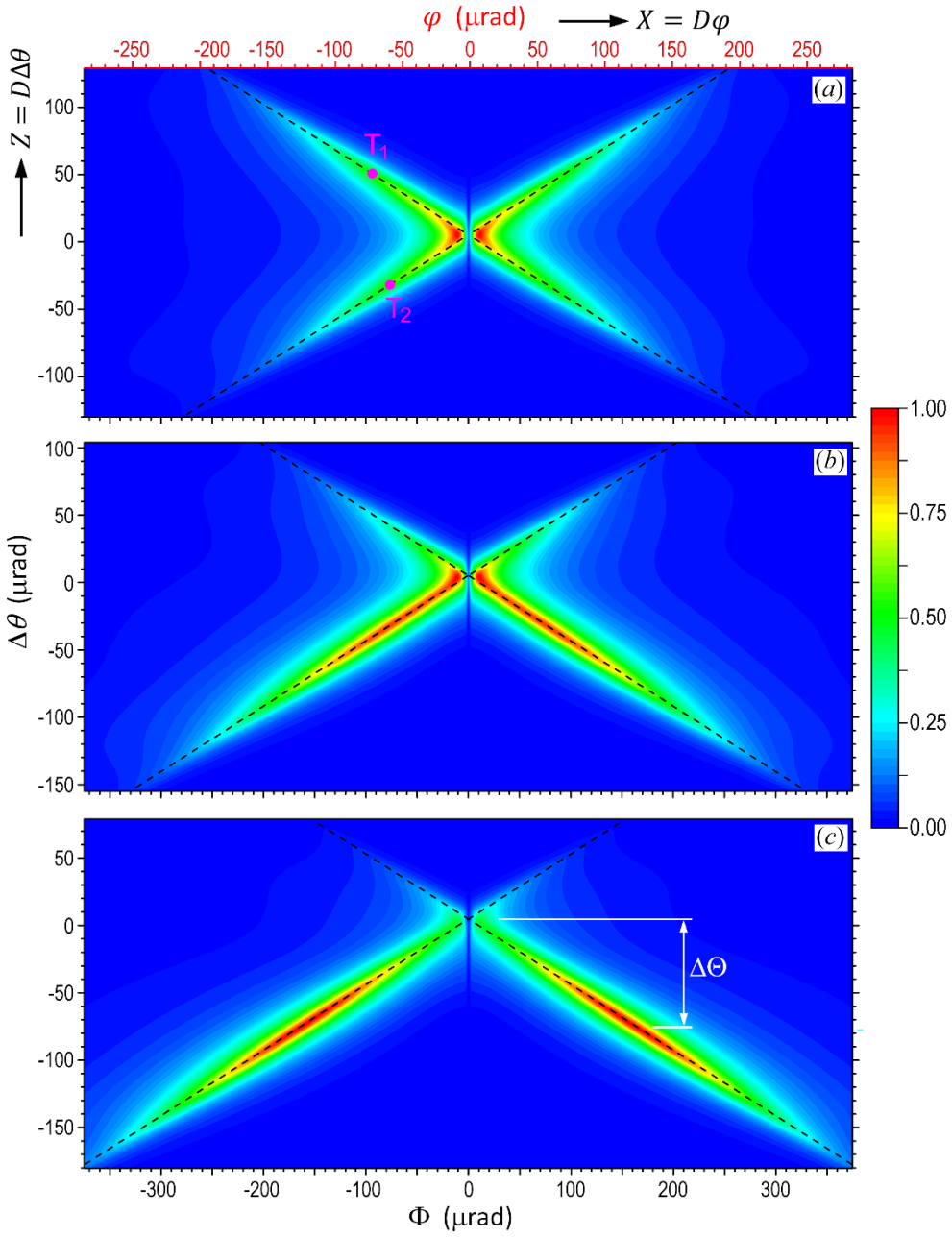

Figure 3. (Two-column figure) Integrated $000/006/113/1\bar{1}3$ 4BD patterns of an incident beam with a Gaussian spectrum (in terms of E). Normalized intensity of the main reflection $\mathbf{g}_1 = 006$. The patterns can be generated with an ideally parallel incident beam by rocking the crystal [2D rocking angles $(\Phi, \Delta\theta)$], or with a divergent beam from a point source as a one-short image in the XZ coordinate system on a CCD [see Fig. 4(a)]. σ-polarization. $\Delta\theta = 0$ always corresponds to $\theta_{4B} = 40.6013°$. The bandwidth (full width at half maximum) of the Gaussian spectrum is 1.5 eV. (a) Central photon energy of the Gaussian spectrum $E_c = E_{4B}$. (b) $E_c = E_{4B} + 0.5$ eV. (c) $E_c = E_{4B} + 1$ eV.

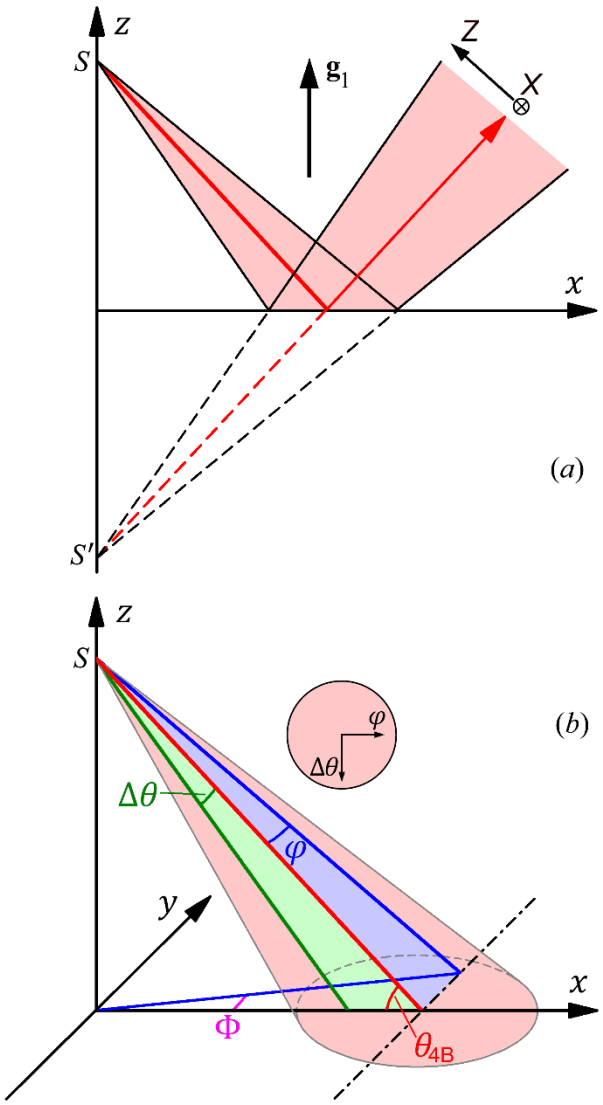

Figure 4. (a) Mirror reflection law of symmetric Bragg reflection. The virtual source S' is exactly the mirror image of the real point source S with respect to the crystal surface ($z = 0$). (b) Relationship between the lateral divergence angle φ and the azimuthal angle Φ on the crystal surface ($z = 0$). Inset indicates the cross section of the divergent beam emitted from the point source, viewed along the direction opposite to the beam direction.

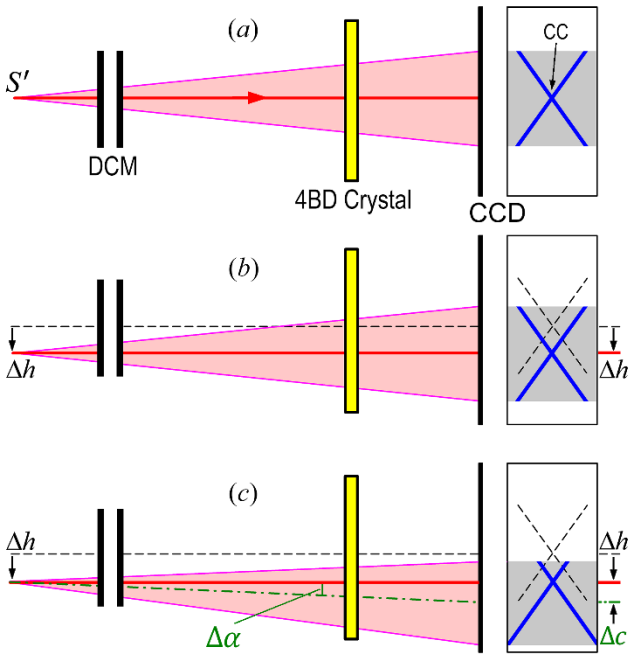

Figure 5. Schematic representation of BPM using 4BD of a point source. Left column shows the side views. Right column shows the CCD viewed along the beam direction ($\mathbf{K}_1$ in Fig. 1). The beam displacement caused by the DCM is not shown, which does not affect the BPM. Since the deflection angle ($2\theta_{4B}$) of the 4BD crystal is omitted, the source S' is the virtual source in Fig. 4(a). For simplicity the 2D variations of the source, the beam and the image are indicated by 1D shifts. (a) Initial 4BD configuration. (b) S' is displaced by Δh without beam direction changes. (c) S' is displaced by Δh together with a beam direction change $\Delta\alpha$, which makes the 4BD pattern asymmetric as the image center is shifted by $\Delta c = D\Delta\alpha$ from the CC.

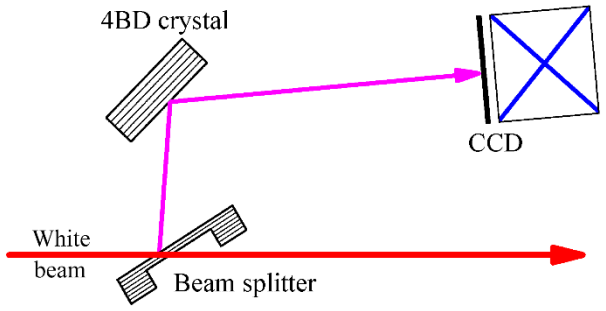

Figure 6. Replacement of the DCM with a thin-crystal window for 4BD-based BMP with possibly low heat load and minimum thermal lattice distortion on the thin crystal. The thin crystal must be of symmetric Bragg reflection.